

Cloud motion and stability estimation for intra-hour solar forecasting

Chi Wai Chow^{a,*}, Serge Belongie^b, Jan Kleissl^a

^a Center for Renewable Resources and Integration, Department of Mechanical and Aerospace Engineering, University of California, San Diego, United States

^b Department of Computer Science, Cornell Tech, New York, United States

Received 23 July 2014; received in revised form 7 March 2015; accepted 15 March 2015

Available online 3 April 2015

Communicated by: Associate Editor David Renne

Abstract

Techniques for estimating cloud motion and stability for intra-hour forecasting using a ground-based sky imaging system are presented. A variational optical flow (VOF) technique was used to determine the sub-pixel accuracy of cloud motion for every pixel. Cloud locations up to 15 min ahead were forecasted by inverse mapping of the cloud map. A month of image data captured by a sky imager at UC San Diego was analyzed to compare the accuracy of VOF forecast with cross-correlation method (CCM) and image persistence method. The VOF forecast with a fixed smoothness parameter was found to be superior to image persistence forecast for all forecast horizons for almost all days and outperform CCM forecast with an average error reduction of 39%, 21%, 19%, and 19% for 0, 5, 10, and 15 min forecasts respectively. Optimum forecasts may be achieved with forecast-horizon-dependent smoothness parameters. In addition, cloud stability and forecast confidence was evaluated by correlating point trajectories with forecast error. Point trajectories were obtained by tracking sub-sampled pixels using optical flow field. Point trajectory length in minutes was shown to increase with decreasing forecast error and provide valuable information for cloud forecast confidence at forecast issue time.

© 2015 Elsevier Ltd. All rights reserved.

Keywords: Sky imager; Solar forecast; Cloud motion tracking; Cloud stability

1. Introduction

Short-term variability in the power generated by solar energy creates challenges for power system planners and operators because of the growing penetration rate. The highly predictable diurnal and annual irradiance pattern aside, clouds have the strongest impact on solar energy production. Transient clouds cause strong spatio-temporal variability and fluctuating solar power feed-into the grid. Large ramp events are of primary concern for relatively small microgrids and island grids, as their ability to absorb the fluctuations is limited. While distributed PV causes less variability to the grid in aggregate, it is less controllable by

grid operators as it often lacks the ability for power curtailment (Eber and Corbus, 2013). The resulting imbalance motivates the need for regulation reserve that scale with both variability and forecast uncertainty (Helman et al., 2010). Different strategies have been studied to mitigate the operational problems with increased solar penetration (Eber and Corbus, 2013; Ela et al., 2013) and a simulation study by Ela et al. (2013) demonstrated that an increased power dispatch frequency and accurate short-term solar forecasts can reduce regulating reserve requirements and production costs. Therefore, reliable forecast information on the expected power production is essential for efficient integration. Since most solar variability (Hoff and Perez, 2012; Lave and Kleissl, 2013), and forecast models (e.g. Chow et al., 2011; Marquez and Coimbra, 2013; Perez et al., 2010) require cloud velocity as main input, accurate

* Corresponding author.

E-mail address: cwchow@ucsd.edu (C.W. Chow).

cloud motion estimation has become of increased interest (Bosch et al., 2013; Bosch and Kleissl, 2013; Fung et al., 2013; Huang et al., 2013; Quesada-Ruiz et al., 2014).

Cloud motion estimation and tracking has a long history in visible satellite imagery (e.g. Menzel, 2001) and solar irradiance forecasts up to a few hours ahead are strongly dependent on the apparent motion of cloud structures. Sparse cloud motion vectors (CMVs) are generally obtained by first locating salient image features such as brightness gradients, corners, cloud edges, or brightness temperature gradients (Bedka and Mecikalski, 2005; Menzel, 2001). Assuming the features do not change significantly over a short interval, CMVs are computed using pattern-matching techniques applied to successive images. The future cloud situation is then estimated by the extrapolation of motion assuming persistence of cloud speed, size, and shape (Lorenz et al., 2004).

CMVs as a basis for advecting such a frozen cloud field derived from ground-based sky imagers were developed and applied by Chow et al. (2011) and Yang et al. (2014). Similar to Hamill and Nehrkorn (1993), the cross-correlation method (CCM) was applied to obtain an average CMV for the entire cloud field. Forecast cloud field position is obtained by shifting the cloud decision images along the corresponding motion vector. Yang et al. (2014) found that CCM advection forecasts (hereinafter CCM forecast) exhibited a larger cloud matching error than image persistence forecast for forecast horizon (FH) of 5 min in 11 of 22 days partially because the spatial homogeneity of the cloud motion assumption is not appropriate given cloud deformation, topographically-induced wind speed variations, and the changing optical perspective. To overcome the above challenges for estimating multiple independent and non-rigid motions, a variational optical flow (VOF) technique is evaluated in this paper. Similar nonrigid registration techniques have also been implemented successfully to estimate cloud motion on sky images last year (Bernecker et al., 2014; West et al., 2014). Optical flow techniques estimate the two-dimensional dense motion field (i.e. every image pixel) with sub-pixel accuracy between two consecutive images (Szeliski, 2010). The variational technique is used in optical flow to minimize an objective function composed of a data model and a regularization term (Horn and Schunck, 1981). The objective function can be solved by well-founded and optimized numerical methods due to the theory of the calculus of variations. As a result of the flexibility of the data modeling process, VOF became a popular technique for motion estimation for fluid imagery such as satellite meteorological images (Corpetti et al., 2002; Héas et al., 2007; Héas and Mémin, 2008) and experimental fluid mechanics (Corpetti et al., 2006; Heitz et al., 2010).

Even though many advanced techniques to estimate cloud motion exist, little attention has been paid on cloud stability, i.e., how rapidly a cloud is changing, which is a key challenge to “frozen” cloud map advection. While time series of cloud fraction and brokenness in the sky imager

field-of-view provide information about the cloud cover variability, changes in these metrics are often dominated by the Eulerian framework (i.e. the advection of clouds in and out of the sky imager field-of-view) and present little information on cloud stability in a Lagrangian sense.

In most cloud advection forecast models, cloud features are assumed constant over the forecast horizon. The validity of this assumption is scale-dependent. Over the sub-30 min forecast horizon of ground-based sky imagery, this assumption often holds for synoptic and even mesoscale cloud systems but is usually violated for individual clouds or small scale features. From highly granular imagery, clouds – especially those located in the atmospheric boundary layer – have often been observed to significantly deform, evaporate, and develop over time scales of a few minutes in the San Diego coastal area (Chow et al., 2011; Yang et al., 2014). Cloud dynamics are driven by cloud and boundary layer turbulence as well as topographic effects and present challenges to deterministic cloud forecasting. Therefore, a method to identify such circumstances and quantify cloud stability is highly desired.

Temporal invariance of cloud features is a characteristic of cloud stability. For that reason, we propose to establish a forecast confidence metric based on dynamic image features and the optical flow field extracted from the VOF method to infer cloud stability and the validity of the frozen-cloud advection technique. In fact, dynamic features have been shown to be of importance in many applications such as object segmentation (Brox and Malik, 2010), cloud classification and synthesis (Liu et al., 2013), and camera calibration (Jacobs et al., 2013).

The main goal in this study is to assess the performance of VOF estimation applied to sky images. In addition, forecast confidence is related to cloud stability through point trajectories that are constructed by tracking pixel points. In Section 2 methods to obtain cloud motion and point trajectories using VOF are described. Section 3 presents results and discussion on cloud forecast and stability. Conclusions follow in Section 4.

2. Methods

2.1. Data

The sky imager developed at UC San Diego (UCSD Sky Imager or “USI”) mainly consists of a charge-coupled device (CCD) image sensor with 12 bits intensity resolution in each RGB channel, a 4.5 mm circular fisheye lens, and a neutral density filter. The USI utilizes high dynamic range (HDR) imaging and outputs lossless PNG images with a bit depth of 16 bits per channel, a dynamic range of 81 dB, and a useable size of the image of 1748×1748 pixels. Images were processed to remove the distortion caused by the fisheye lens, resulting in red–blue-ratios (RBRs) in a Cartesian coordinate system at the predetermined cloud height. Complete specifications of the USI system can be found in Urquhart et al. (2013, 2014). The November

2012 data consists of images captured every 30 s as studied by Yang et al. (2014). Images were not considered if they were clear (cloud fraction <5%) or overcast (>95%). A summary of the sky conditions for each day is shown in Table A.1 in the appendix. To illustrate the sensitivity of the regularization term in the VOF method and point trajectory method, image sequences on November 10 and 14, 2014 will be used. November 10 consists of mainly cumulus clouds with well-defined edges and large pixel displacement of motion, while November 14 consists of smooth, homogenous cirrus clouds with small pixel displacement.

2.2. Motion estimation

2.2.1. Variational optical flow forecast (VOF forecast)

The fundamental assumption behind optical flow is that an image pixel values does not change over consecutive frames, but only shift position. Mathematically:

$$I_t(x_t, y_t) = I_{t+1}(x_t + u_t(x_t, y_t), y_t + v_t(x_t, y_t)), \quad (1)$$

where I represents pixel values, such as color (R, G and B) or gray scale intensity, x_t and y_t are the Cartesian pixel indices, and $u_t(x_t, y_t)$ and $v_t(x_t, y_t)$ are the motion vector components for pixel (x_t, y_t) in frame t . The goal is to compute the optical flow field $\{u_t(x_t, y_t), v_t(x_t, y_t)\}$ between two successive frames of an image sequence. The brightness constancy equation is a nonlinear equation in u and v . To simplify the nonlinear equation and solve for the optical flow field, the equation is linearized by a first order Taylor expansion leading to the well-known optical flow constraint (OFC) equation

$$0 = \frac{\partial I}{\partial t} + \frac{\partial I}{\partial x}u + \frac{\partial I}{\partial y}v. \quad (2)$$

The OFC equation is often violated in a realistic cloud scene due to changing illumination, occlusion, non-Lambertian reflectance, etc. For example, clouds in proximity to the sun are whiter than in other locations due to forward scattering and this leads to significant deviations from the brightness constancy assumption. Therefore, to remove the sun-pixel-angle dependence of pixel intensity, a residual red-to-blue ratio (RBR) (RBR image subtracted by the clear sky background RBR image) is used in this study to represent I to correct for background heterogeneity. Clouds are known to leave stronger signatures in the red channel (Shields et al., 2013) and normalization by the blue channel contributes to normalizing out general brightness deviations.

The OFC is an ill-posed problem, i.e. an under-determined system that has one equation with two unknowns, u and v , for which a unique motion cannot be recovered locally without additional constraints. An early approach to handle the OFC problem, known as the local method, was proposed by Lucas and Kanade (1981). They evaluated the OFC equation within a neighborhood where the flow field is assumed homogenous. Nevertheless, choosing

an appropriate neighborhood size is challenging and this approach does not solve the ambiguity in homogenous regions. Horn and Schunck (1981) proposed another method based on the assumption that the optical flow field is similar locally and spatially smooth for the whole image. They minimized an objective function by using brightness constancy and global smoothness as model assumptions in a variational method.

In a variational method, model assumptions $S_1 + \dots + S_m$ are formulated in terms of an energy functional

$$E(f_1(\omega), \dots, f_n(\omega)) = \int (S_1 + \dots + S_m) d\omega \quad (3)$$

and the functions $f_1(\omega), \dots, f_n(\omega)$ should minimize the energy E , where $\omega = (x, y)$ denotes a point in the image domain. In this research, the algorithm by Liu (2009) is used due to its simple implementation, relatively low computational intensity, and flexibility in parameters. The global deviations from the brightness constancy and smoothness assumption are measured by

$$E(u, v) = \int \phi(I_t(x_t, y_t) - I_{t+1}(x_t + u, y_t + v)) d\omega + \alpha \int \phi(|\nabla_2 u|^2 + |\nabla_2 v|^2) d\omega, \quad (4)$$

where α is a parameter that weighs the second term (regularization term) relative to the OFC term, ∇ is the gradient operator, and ϕ is a robust function (Black and Anandan, 1996). The regularization term models the spatial smoothness of the optical flow and penalizes high variation across an image. The goal is to find the optical flow field u and v that minimizes E .

In addition to the variational approach, a multi-scale approach is used to avoid local minima of energy. If displacements between two images are large, the first order Taylor expansion of the brightness constancy equation becomes invalid and the solution of the energy function (Eq. (4)) can be trapped in a local minimum. To avoid such situations, the multi-scale approach initializes the energy minimization in Eq. (4) on a coarse scale to find the global minimum and propagates the solution gradually to the finer scale. Finally, the theory of the calculus of variations leads to a system of Euler–Lagrange equations and they are solved by successive over-relaxation (SOR) numerical approximation. Details on minimization of the energy and the numerical approximation can be found in Brox (2005) and Liu (2009).

To shift the cloud map with the motion vector field the optical flow method obtains pixel positions with a heterogeneous flow field $u_t(x_t, y_t)$ and $v_t(x_t, y_t)$. In general, there are two ways to warp an image: forward and inverse mapping. Let $U(x, y)$ and $V(x, y)$ be a mapping by the optical flow field between coordinate (x, y) and (x', y') . For forward mapping, each coordinate pair (x, y) in the source image is copied to the output image location (x', y') or in vector notation as

$$\begin{pmatrix} x' \\ y' \end{pmatrix} = \begin{pmatrix} U_f(x, y) \\ V_f(x, y) \end{pmatrix} \quad (5)$$

The primary limitation of forward mapping is that it produces holes and overlapped pixels in the output image that need to be handled with interpolation and averaging. Therefore, inverse mapping is used to warp the image and is expressed as

$$\begin{pmatrix} x \\ y \end{pmatrix} = \begin{pmatrix} U_i(x', y') \\ V_i(x', y') \end{pmatrix}. \quad (6)$$

Inverse mapping scans through each output pixel and samples the correct input pixel from the source image. In this way, every pixel in the output image is guaranteed to be mapped to a pixel from the source image.

2.2.2. Cloud forecast metrics

To evaluate the VOF forecast, the VOF forecasts of the binary cloud decision of a sky image transformed to Cartesian coordinates (hereinafter cloud map) is compared against the CCM forecasts described in Chow et al. (2011). The nowcast (i.e. 0 min forecast) is obtained by shifting the cloud map at time $t_0 - dt$ ($dt = 30$ s throughout this analysis) with the motion vector field determined from the VOF and CCM applied to the images at time t_0 and $t_0 - dt$ (Fig. 1). While the nowcast performance is not of practical relevance since “future” information is used in generating the nowcast, it serves as a useful benchmark since the assumption of cloud speed persistence is not required. To forecast cloud maps at horizons greater than 0 min, the cloud map at time t_0 is advected with the motion vector field to the forecast horizon. To determine accuracy, the actual cloud map at time $t_0 + n \cdot dt$ is overlaid onto the advected cloud map to determine the pixel-by-pixel forecast error. This matching error between the two cloud maps is

$$e_m = \frac{P_{\text{false}}}{P_{\text{total}}} \times 100\%, \quad (7)$$

which is the ratio between the number of falsely forecasted pixels and the number of total pixels in the image. The

matching error is sensitive to cloud fraction. Therefore the cloud-advection-versus-persistence (cap) error

$$e_{\text{cap}} = \frac{P_{\text{false, advection}}}{P_{\text{false, persistent}}} \times 100\% \quad (8)$$

is applied to measure if cloud advection improves over a naïve image persistence forecast. The forecast skill (FS)

$$\text{FS} = 1 - \frac{e_{m, \text{VOF}}}{e_{m, \text{CCM}}} \quad (9)$$

is defined to measure the improvement in the matching error of the VOF forecast compared to the CCM forecast. Positive values of FS indicate that the VOF forecast is superior to the CCM forecast, with a maximum possible value of one. Since the two advection methods produce spatially different forecast maps, only the common points are compared in both metrics.

2.3. Point trajectories and forecast confidence

Point trajectories are obtained by developing an optical flow tracker based on Sundaram et al. (2010). Tracking points are initialized (sub-sampled) every twenty pixels from the first frame of an image sequence. Points located in homogenous (e.g. clear or overcast) regions are difficult to track and are therefore removed. Homogeneous regions are identified by the second eigenvalue of the structure tensor, $J_o = \sum_{i=1}^2 \nabla I_i \nabla I_i^T$ (hereinafter image structure) (Sundaram et al., 2010). Each of the points is then tracked using the optical flow field

$$(x_{t+1}, y_{t+1}) = (x_t, y_t) + (u_t(x_t, y_t), v_t(x_t, y_t)). \quad (10)$$

Tracking of a point is terminated if one of the following three circumstances is encountered:

1. Point is advected out of the forecast domain.
2. Forward and backward optical flow yield inconsistent results (Sundaram et al., 2010). Tracking is stopped if the inconsistency is larger than a threshold, which varies as a linear function of motion magnitude.
3. The image structure around the trajectory point decreases. The local image structure can capture the dynamics of the cloud evolution as, for example, cloud evaporation decreases the local RBR gradient. However, image structure can also decrease due to measurement errors or optical effects; for example, clouds moving into the solar region appear to have less structure due to pixel saturation.

Lastly, to fill the empty areas due to terminated trajectories, new tracks are initialized in unoccupied areas in each new frame. The trajectory length represents the duration of a pixel point that stays in an image sequence, and the average time length of terminated trajectories for a frame, \bar{T}_{len} , is used to quantify cloud stability. Since clouds entering the field-of-view of the sky imager are by default associated with a shorter trajectory length, a

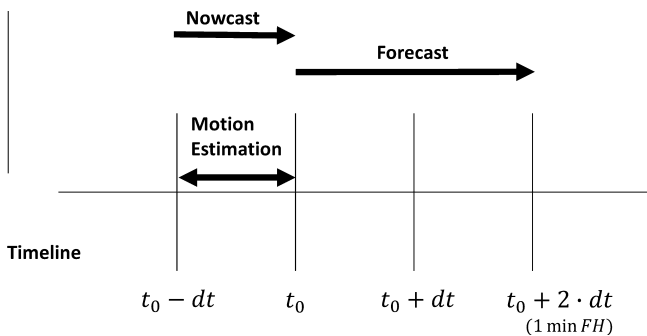


Fig. 1. Timeline for nowcasting and forecasting the cloud map. $dt = 30$ s throughout this study.

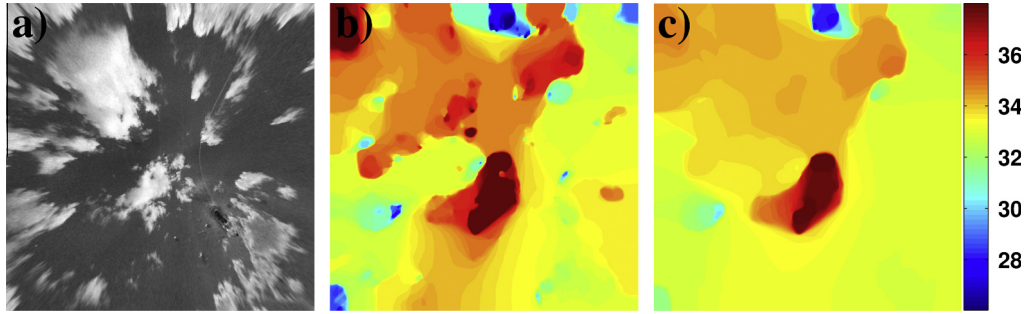


Fig. 2. Optical flow estimation of the residual RBR image on November 10th, 2012, 08:46:00 PST out to zenith angles of 75° (a) with spatial smoothness $\alpha = 0.01$ (b) and $\alpha = 0.1$ (c). The colorbar indicates the motion magnitude in pixel per frame. (For interpretation of the references to color in this figure legend, the reader is referred to the web version of this article.)

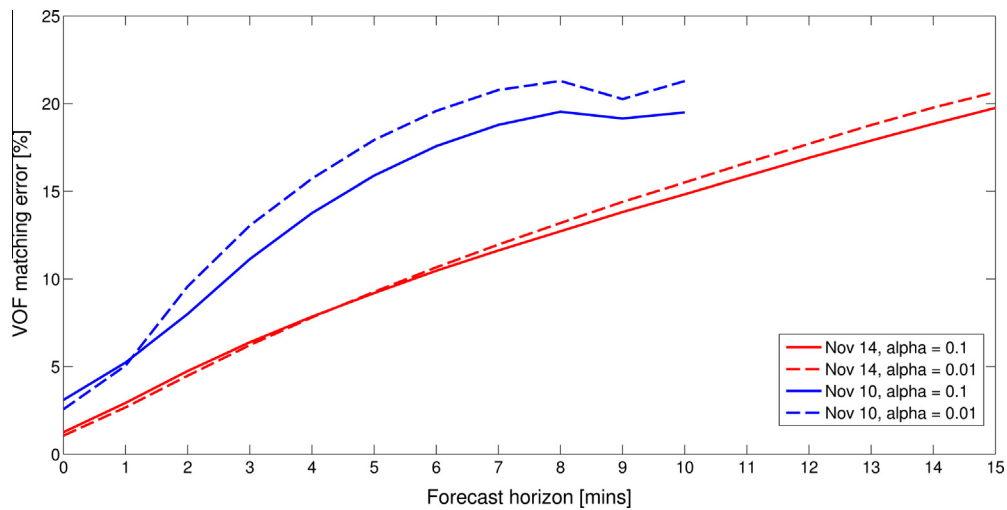


Fig. 3. Cloud forecast performance for November 10 (cumulus) and 14, 2012 (cirrus clouds) with smoothness $\alpha = 0.01$ and 0.1. Cloud matching error for FH beyond 10 min is not shown for November 10 since more than 70% of the cloud map is advected out of the USI field-of-view.

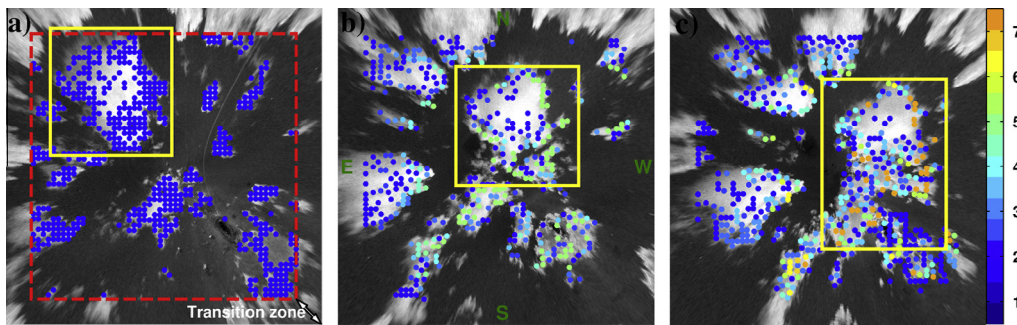


Fig. 4. A set of points is initialized with a sub-sampled grid on a residual RBR image (a) and tracked for 5 min or 10 frames with $\bar{T}_{len} = 3.18$ min (b) and 7.5 min or 15 frames with $\bar{T}_{len} = 3.79$ min (c) on November 10th, 2012. For ease of following the cloud motion the largest cloud is demarcated by the yellow box. While the sequence illustrated here begins at 16:46:00 UTC, the point trajectory method is implemented at the beginning of each day when solar zenith angle (SZA) $< 75^\circ$. Trajectories are initialized everywhere but \bar{T}_{len} (colorbar) is not counted in the transition zone (as indicated by the red dashed box) to avoid \bar{T}_{len} being biased low from new clouds entering the forecast domain. The colorbar indicates the point trajectory length in minutes. (For interpretation of the references to color in this figure legend, the reader is referred to the web version of this article.)

marginal space/transition zone is used between the image domain and region of interest (see Fig. 4 later) and the trajectories in the transition zone are not considered in \bar{T}_{len} . Furthermore, the minimum value of \bar{T}_{len} is 1 min as newly initialized tracks are not considered in the average.

3. Experimental results and discussion

3.1. Cloud forecast

Fig. 2b shows an example image demonstrating the ability of the optical flow technique to capture the non-uniform

cloud motion. The cloud in the center moves about 10% faster than the clouds in the east and south areas of the forecast domain. Table 1 shows a summary of the CCM and VOF forecast performance for each partly cloudy day in November 2012 using the error metrics introduced in Section 2. For the 0 min forecast (nowcast), FS is positive for all days, which confirms that the VOF method is better able to estimate the motion than CCM.

Since the average FS for 5, 10, and 15 min horizons is 0.21, 0.19, and 0.19 respectively, the VOF forecast performed better than CCM forecast on average. The VOF forecast is superior to the CCM forecast for 5 and 10 min FHs for all days. The VOF forecast also outperformed image persistence forecast ($e_{\text{cap,VOF}} < 100$) for the 5–15 min FHs for more than 18 out of 20 days, but less than half of the days for the CCM forecast. For the 15 min forecast, the cloud map is always advected out of 70% of the sky imager field-of-view on 8 days (resulting in missing entries in Table 1) revealing the general limitation of sky imager forecast for FH beyond 15 min. For most days, the FS decreases with increasing FH. We believe that errors not related to cloud motion equally increase the matching error of both methods with longer FH, resulting in a larger matching error ratio and smaller FS. Examples of such errors are cloud decision errors and violations of the frozen cloud map assumption, such as perspective errors (Yang et al., 2014).

For the remainder of the manuscript only the VOF technique is considered and the ability to track points with the VOF technique is exploited to quantify correlations between cloud forecast accuracy and cloud stability.

3.1.1. Sensitivity to VOF smoothness

The optical flow estimation result with two different smoothness parameters α (Eq. (4)) is shown in Fig. 2. As expected, more spatial variations of cloud motion and sharper motion boundaries are observed for a smaller α . The larger α yields a smoother flow field with a tradeoff of possible less accurate local flow estimation.

VOF forecast from a less smoothed flow field ($\alpha = 0.01$) is shown to perform better for FH of 1 and 5 min for November 10 and November 14, respectively (Fig. 3). The less smoothed flow field better captured the small-scale motion near the cloud edge and forecasts more accurately for a very short forecast horizon. Yet, the physical lifetime of these small scales is usually only a few minutes after which they become unpredictable leading to deviations from the frozen cloud map assumption and larger forecast errors as the forecast horizon increases. Especially for the cumulus case (November 10) cloud turbulence is stronger and small scales are expected to have shorter life times leading to the earlier cross-over between the different smoothness parameters in Fig. 3. This implies that the optimal cloud motion field should be smooth enough to avoid extrapolating localized motion beyond its lifetime, yet able to capture spatially heterogeneous cloud motion. Therefore, a FH-dependent smoothness parameters may be advantageous to yield the optimum forecast over all time horizons, at least for days with boundary layer clouds that are associated with turbulent motion on a large range of time scales. However, the implementation of such a procedure would require significant fine tuning and was

Table 1

Summary of cap errors and forecast skill for 0, 5, 10, and 15 min forecast horizon for 20 days in November 2012. The errors are only computed under partly cloudy conditions ($5\% < \text{cloud fraction} < 95\%$) only. Asterisks mark cases when the cloud map was advected more than 70% out of the USI field-of-view on average.

Date	$e_{\text{cap,CCM}}$ (%)				$e_{\text{cap,VOF}}$ (%)				FS (–)			
	Forecast horizon (min)											
	0	5	10	15	0	5	10	15	0	5	10	15
11/01	59.5	91.2	108.7	118.0	37.4	59.4	75.9	85.7	0.37	0.35	0.30	0.27
11/02	96.6	110.4	120.7	122.5	54.4	68.5	76.9	84.3	0.44	0.38	0.36	0.31
11/03	112.0	102.1	100.0	100.0	77.0	85.9	95.0	111.0	0.31	0.16	0.05	–0.11
11/07	93.5	252.8	*	*	70.9	89.0	*	*	0.24	0.65	*	*
11/08	63.3	87.6	112.3	124.8	42.0	61.1	76.1	87.3	0.34	0.30	0.32	0.30
11/09	50.3	76.1	80.1	*	28.7	58.4	65.7	*	0.43	0.23	0.18	*
11/10	35.4	63.4	*	*	23.8	53.6	*	*	0.33	0.16	*	*
11/14	44.8	60.8	73.9	87.7	24.5	40.5	52.5	65.5	0.47	0.30	0.23	0.16
11/16	44.1	60.3	69.8	56.9	24.3	45.9	58.8	50.4	0.45	0.24	0.16	0.11
11/17	55.4	86.6	107.0	123.0	33.4	63.3	82.3	94.2	0.40	0.27	0.23	0.23
11/18	101.9	101.0	*	*	58.6	82.5	*	*	0.43	0.18	*	*
11/20	74.9	97.3	99.6	*	70.5	83.4	89.6	*	0.06	0.14	0.10	*
11/21	76.4	98.4	96.7	*	49.2	65.2	72.4	*	0.36	0.34	0.25	*
11/22	96.0	428.5	*	*	62.3	197.5	*	*	0.35	0.54	*	*
11/23	100.0	100.0	100.0	100.0	76.4	80.0	81.9	82.1	0.24	0.20	0.18	0.18
11/24	100.4	100.5	99.4	97.5	76.9	78.6	85.0	84.4	0.23	0.22	0.14	0.13
11/25	93.0	310.7	388.1	*	58.6	126.1	196.5	*	0.37	0.59	0.49	*
11/26	87.4	130.3	125.8	132.9	47.6	71.3	82.3	94.1	0.46	0.45	0.35	0.29
11/27	47.0	46.5	43.2	45.7	26.9	29.4	28.3	31.0	0.43	0.37	0.35	0.32
11/28	225.5	468.7	345.4	381.5	58.9	61.8	64.6	68.1	0.74	0.87	0.81	0.82
Mean									0.39	0.21	0.19	0.19

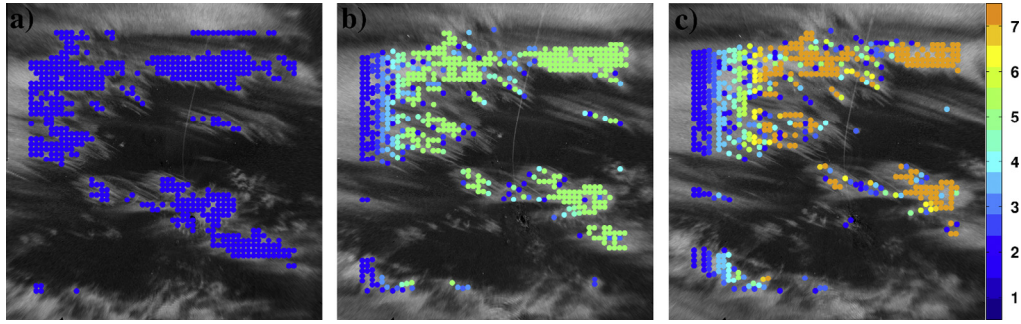


Fig. 5. A set of points is initialized (a) and tracked for 5 min or 10 frames with $T_{\text{len}} = 4.38$ min (b) and 7.5 min or 15 frames with $T_{\text{len}} = 6.71$ min (c) on November 14th, 2012 at 18:00:00 UTC. Cirrus clouds were observed to be stable with almost constant image structures that yield long trajectory points.

beyond the scope of this paper and $\alpha = 0.1$ was used for the remainder of manuscript.

3.2. Cloud stability

The tracking result of an image sequence of cumulus clouds on November 10 is illustrated in Fig. 4. A set of points on a regular grid was initialized in areas with high image structure (see beginning of Section 2.3). High image

structure exists primarily in partly cloudy conditions, while image structure is small in clear sky region and homogeneous cloud areas (Fig. 4a). Points were tracked from frame to frame according to the optical flow field to construct point trajectories. In Fig. 4b, nearly half of the points had been tracked for 5 min (light green color), while the remaining points have a shorter trajectory length (blue) due to cloud break-up (yellow box of Fig. 4b) and formation and entering the sky imager field of view. Only a small

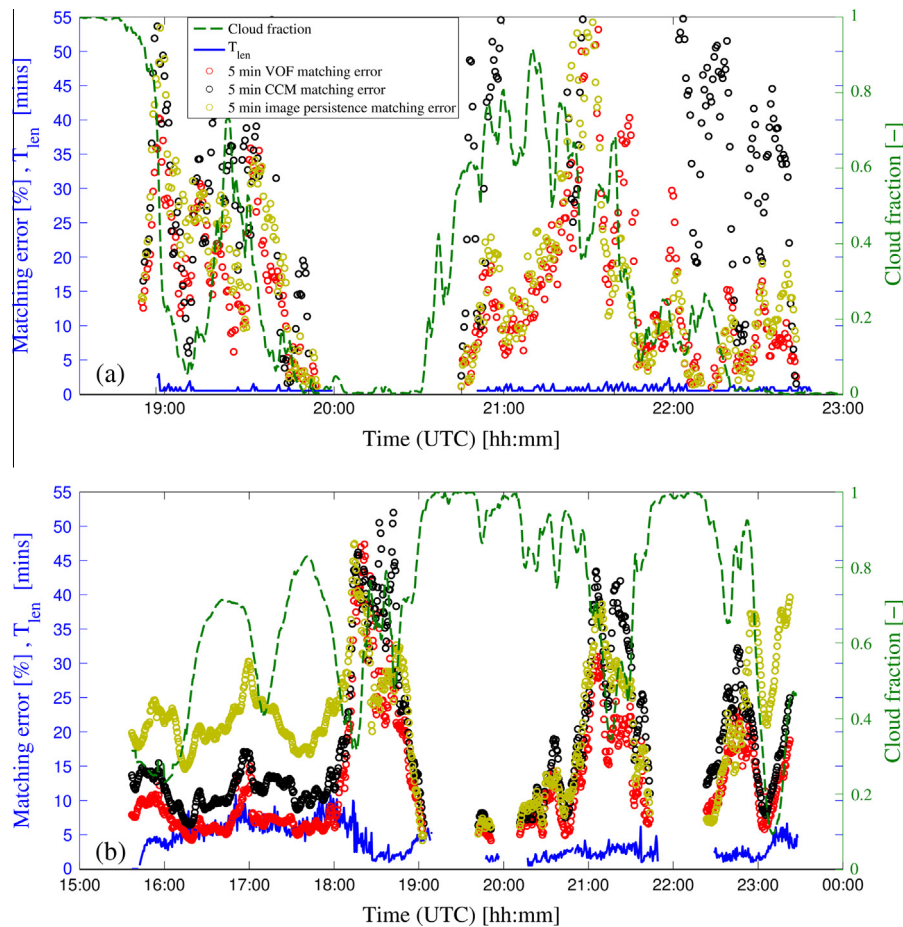


Fig. 6. Time series of cloud matching error e_m for VOF and image persistence, average trajectory length \bar{T}_{len} , and cloud fraction on November 7, 2011 (a), and November 8, 2011 (b). Large and small cloud fractions are typically associated with small matching errors.

fraction of points were tracked for 7.5 min (Fig. 4c) and two clouds were merging to form a larger cloud (yellow box of Fig. 4c). In this image sequence, the longest point trajectories (orange color) are associated with the largest cloud from the first frame. Generally, large clouds were observed to have longer point trajectories presumably since they are thicker on average and therefore contain more liquid water. Therefore cloud evaporation and deformation requires more energy and time, which results in less change of appearance.

The tracking result of an image sequence of cirrus clouds on November 14 is shown in Fig. 5. This image sequence presented temporally stable clouds without deformation and with uniform motion across the sky. Only a small fraction of points were terminated and not tracked to for 7.5 min (Fig. 5c).

Using the point trajectory technique described in Section 2.3, point trajectory lengths were sampled at the forecast issue time on the 20 days listed in Table 1. To investigate the relationship between point trajectories lengths and cloud stability, time series plots of VOF matching error, cloud fraction, and average trajectory length \bar{T}_{len}

for 5 min forecast of two different days are presented in Fig. 6. While the cloud matching error is presented at forecast valid time, the trajectory length sampled at forecast issue time is shifted to the forecast valid time to facilitate comparison. November 7 (Fig. 6a) illustrates a day with poor forecast accuracy (cap error of 89%). Starting at 1900 UTC highly variable cumulus clouds are observed in the sky images (not shown here) which is reflected in the short trajectory length ($\bar{T}_{len} = 1.18$ min). Therefore, image persistence and VOF forecasts performed similarly on this day.

On the other hand, on November 8 multiple cloud layers are observed. Between 1600 and 1800 UTC stable altocumulus and cirrus clouds brought forth a \bar{T}_{len} between 2 and 10 min (Fig. 6b). Cloud-advection outperformed persistence forecast during this period as indicated by the smaller matching error. Shallow cumulus clouds along with altocumulus clouds were predominant from 2000 UTC until 2300 UTC. \bar{T}_{len} is between 1 and 5 min and persistence and cloud advection forecasts performed similarly. From 2300 UTC until sunset, single layer altocumulus clouds with a trajectory length around

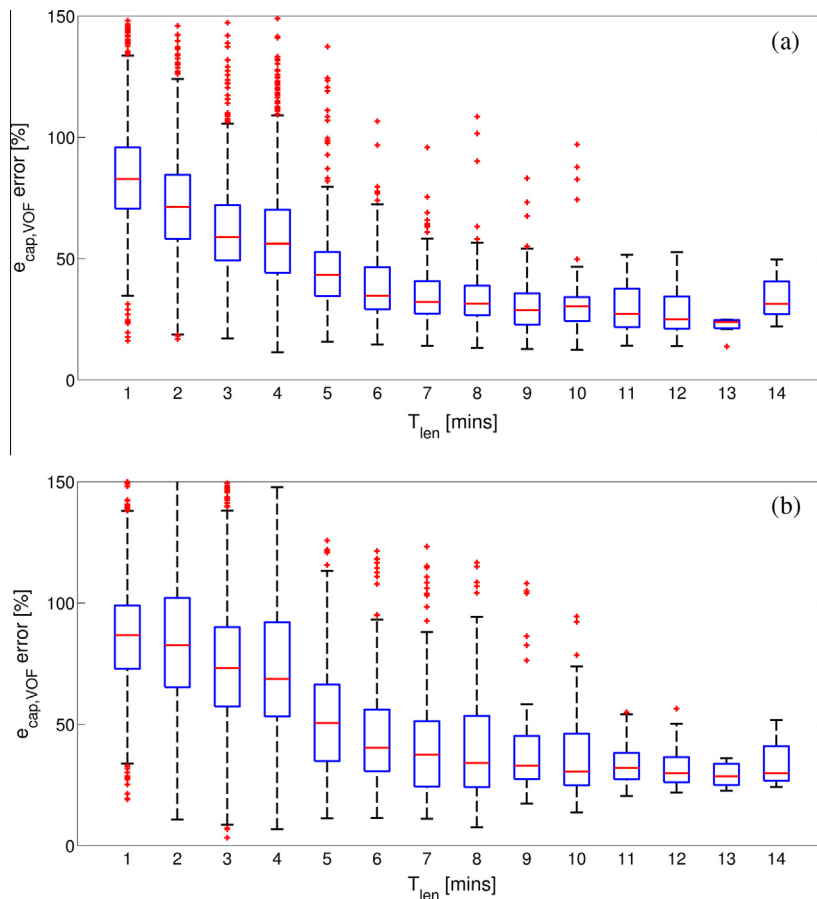


Fig. 7. Boxplot of VOF cap error as a function of average trajectory length T_{len} for 5 min (a) and 10 min (b) forecast horizons. Red lines and dots indicate the median and outliers respectively. The top and bottom of the box shows the 75th and 25th percentile. The end of the whisker marks the value of the data set that are within 1.5 times the interquartile range.

Table 2

Daily 5-min cap errors of VOF forecasts and average trajectory length. No trajectory length greater than 1 min is observed on November 28 due to false cloudy sky caused by inaccurate cloud decision.

	$e_{\text{cap,VOF}}$ (%)	\bar{T}_{len} (min)		$e_{\text{cap,VOF}}$ (%)	\bar{T}_{len} (min)
November 01	59.4	3.13	November 18	82.5	1.56
November 02	68.5	2.41	November 20	83.4	1.17
November 03	85.9	1.16	November 21	65.2	2.76
November 07	89.0	1.18	November 22	197.5	1.35
November 08	61.1	4.05	November 23	80.0	1.04
November 09	58.4	3.02	November 24	78.6	1.05
November 10	53.6	2.95	November 25	126.1	2.62
November 14	55.8	4.57	November 26	71.3	3.33
November 16	45.9	4.74	November 27	29.4	8.57
November 17	63.3	3.72	November 28	61.8	NaN

5 min allowed cloud advection to outperform persistence again. These observations indicate a correlation of the point trajectory length with cloud stability and cap error.

To determine the general applicability of trajectory length as a forecast confidence metric for an operational forecast setting, boxplots of 5 and 10 min cap error against average trajectory length for all days are presented in Fig. 7. The results indicate that both 5 and 10 min cap errors decrease as \bar{T}_{len} increases. For 5 min forecasts, VOF forecast began to perform 50% better (as measured by the median) than image persistence for trajectory lengths of 5 min. For 10-min VOF forecast to outperform 50% persistence, a minimum length of 6 min is required. It is expected that the critical trajectory length for VOF to outperform persistence increases with forecast horizon, as the frozen cloud assumption must hold over the forecast horizon. While the critical trajectory length may be expected to be larger than the forecast horizon, it is important to note that many trajectory points may terminate due to small scale deformation of the cloud, while the large scale feature of the cloud will remain intact and is most relevant for cap error.

Table 2 summarizes daily 5 min cap errors along with \bar{T}_{len} . For the 8 out of 20 days that have cap error greater than 75%, the average \bar{T}_{len} is 1.53 min, while it averages 3.93 min for the remaining days. The results indicate that trajectories are longer ($\bar{T}_{\text{len}} > 2$ min) for days when cloud advection improves 25% over image persistence forecast confirming the hypothesis that short trajectories imply unstable clouds. However, the daily averaged values may not be representative since cloud conditions often vary during the day (e.g. November 8 in Fig. 6b).

4. Conclusion

Techniques for dense motion estimation and point trajectories were presented. A month of image data

captured by a sky imager at UC San Diego was analyzed to determine the accuracy of variational optical flow (VOF) forecasts and infer cloud stability. Cloud-advection was based on motion estimation between successive frames that are 30 s apart. The VOF method not only resulted in better motion estimation (0 min forecasts), it was also able to produce accurate cloud forecasts (>0 min) by capturing multiple independent cloud motions while maintaining a spatially smooth motion field across an image. The VOF forecast was found to be superior to CCM forecast for with an average error reduction of 39%, 21%, 19%, and 19% for 0, 5, 10, and 15 min forecasts respectively. While image persistence outperformed VOF forecast for forecast horizons of 5 and 10 min on 2 out of 20 days these days were associated with highly variable clouds that make any cloud advection approach challenging.

The VOF analysis demonstrated that unstable clouds make accurate cloud motion forecasts impossible and such conditions need to be identified to quantify forecast confidence. Cloud stability was successfully quantified using point trajectory lengths by tracking points in an image sequence to form trajectories. Trajectory lengths were correlated with forecast cap errors for both daily averaged metrics and individual forecast realizations. Consequently, short trajectory lengths are associated with large cap error of VOF forecast (or low confidence), while long trajectory lengths and small matching errors were related to high cloud stability. The VOF forecast was found to be 50% superior to image persistence forecast for 5 and 10 min forecast horizons with a minimum trajectory length of 5 and 6 min respectively. Point trajectory length was proven to be a valuable forecast confidence and cloud stability metric that can provide information on the applicability of the frozen cloud map assumption at forecast issue time.

Appendix A

See Table A.1.

Table A.1

Summary of sky conditions listed chronologically. Sky conditions joined by an ampersand indicate simultaneous occurrence. All times in PST (UTC – 8 h) (adapted from Yang et al. (2014) with permission).

Date	Morning (7:00–9:59)	Midday (10:00–12:59)	Afternoon (13:00–16:00)
November 1, 2012	OVC	Cu-EF	CLR, Ci
November 2, 2012	OVC, Cu-EF	CLR	CLR
November 3, 2012	CLR	CLR, Cu	Cu
November 4, 2012	CLR	CLR	CLR
November 5, 2012	CLR	CLR	CLR
November 6, 2012	CLR, Fog (brief)	CLR	CLR
November 7, 2012	OVC	Cu-EF	Cu-EF
November 8, 2012	Ci, Ac	Cu-EF and Ac	Cu and Ac
November 9, 2012	Cu and Ac, Ac	Ac, Cu and Ac	Cu-EF
November 10, 2012	Cu	Cu-EF	Cu-EF, CLR
November 11, 2012	CLR	CLR	CLR
November 13, 2012	CLR	CLR	CLR
November 14, 2012	Ci	Ci, Cc	Cc
November 15, 2012	OVC	OVC	OVC
November 16, 2012	Ac, CLR	CLR, Ac, CLR	CLR, Ac
November 17, 2012	Cu-EF	Cu-EF	Ac
November 18, 2012	OVC, Cu-EF and Ac	Cu-EF, Ci, Cu and Ci	Cu
November 19, 2012	CLR	CLR	CLR, Cu
November 20, 2012	CLR	CLR	Cu
November 21, 2012	OVC	Cu-EF, CLR	CLR
November 22, 2012	Fog, Cu-EF	≈CLR	Cu-EF
November 23, 2012	OVC	CLR, Cu-EF, CLR	CLR, Cu-EF, OVC
November 24, 2012	CLR	CLR	CLR, Cu, Haze
November 25, 2012	OVC	OVC, Cu-EF, CLR	CLR, Cu, CLR
November 26, 2012	Cu-EF	CLR, Cu-EF, Cu-EF and Ci	Cu-EF and Ci
November 27, 2012	OVC	Cu-EF and Ci, Ci	Cc, Cc and Cu, OVC
November 28, 2012	OVC	Cu-EF, Haze	CLR
November 29, 2012	OVC	OVC	OVC, Ac
November 30, 2012	OVC	Cu-EF and Ac, OVC	OVC
December 1, 2012	OVC, Cu-EF and Ci	Cu-EF and Ci	Ci, Cu and Ci
December 2, 2012	OVC	OVC, Cu	CLR

CLR: clear sky. Cloud fraction <5%.

OVC: overcast. Cloud fraction >95%.

EF: denotes periods of prominent cloud evaporation and formation.

Cu: cumulus clouds. Low-level (<2 km) clumpy clouds with sharp edges.

Ac: altocumulus clouds. Mid-level (2–6 km) clumpy clouds with sharp edges.

Cc: cirrocumulus clouds. High-level (>6 km) clumpy clouds with sharp edges.

Ci: cirrus clouds. High-level (>6 km) thin, wispy clouds.

References

- Bedka, K.M., Mecikalski, J.R., 2005. Application of satellite-derived atmospheric motion vectors for estimating mesoscale flows. *J. Appl. Meteorol.* 44 (11), 1761–1772.
- Bernecker, D., Riess, C., Angelopoulou, E., Hornegger, J., 2014. Continuous short-term irradiance forecasts using sky images. *Sol. Energy* 110, 303–315.
- Black, M.J., Anandan, P., 1996. The robust estimation of multiple motions: parametric and piecewise-smooth flow fields. *Comput. Vis. Image Underst.* 63 (1), 75–104.
- Bosch, J.L., Kleissl, J., 2013. Cloud motion vectors from a network of ground sensors in a solar power plant. *Sol. Energy* 95, 13–20.
- Bosch, J.L., Zheng, Y., Kleissl, J., 2013. Deriving cloud velocity from an array of solar radiation measurements. *Sol. Energy* 87, 196–203.
- Brox, T., 2005. From pixels to regions: partial differential equations in image analysis (Doctoral dissertation).
- Brox, T., Malik, J., 2010. Object segmentation by long term analysis of point trajectories. *Computer Vision – ECCV 2010*. Springer, Berlin Heidelberg, pp. 282–295.
- Chow, C.W., Urquhart, B., Lave, M., Dominguez, A., Kleissl, J., Shields, J., Washom, B., 2011. Intra-hour forecasting with a total sky imager at the UC San Diego solar energy testbed. *Sol. Energy* 85 (11), 2881–2893.
- Corpetti, T., Mémén, É., Pérez, P., 2002. Dense estimation of fluid flows. *IEEE Trans. Pattern Anal. Mach. Intell.* 24 (3), 365–380.
- Corpetti, T., Heitz, D., Arroyo, G., Mémén, E., Santa-Cruz, A., 2006. Fluid experimental flow estimation based on an optical-flow scheme. *Exp. Fluids* 40 (1), 80–97.
- Eber, K., Corbus, D., 2013. Hawaii Solar Integration Study: Executive Summary.
- Ela, E., Diakov, V., Ibanez, E., Heaney, M., 2013. Impacts of Variability and Uncertainty in Solar Photovoltaic Generation at Multiple Timescales (No. NREL/TP-5500-58274). National Renewable Energy Laboratory (NREL), Golden CO.
- Fung, V., Bosch, J.L., Roberts, S.W., Kleissl, J., 2013. Cloud speed sensor. *Atmos. Meas. Tech. Discuss.* 6 (5), 9037–9059.
- Hamill, T.M., Neherkorn, T., 1993. A short-term cloud forecast scheme using cross correlations. *Weather Forecast.* 8 (4), 401–411.
- Héas, P., Mémén, E., Papadakis, N., Szantai, A., 2007. Layered estimation of atmospheric mesoscale dynamics from satellite imagery. *IEEE Trans. Geosci. Remote Sens.* 45 (12), 4087–4104.
- Héas, P., Mémén, E., 2008. Three-dimensional motion estimation of atmospheric layers from image sequences. *IEEE Trans. Geosci. Remote Sens.* 46 (8), 2385–2396.

- Heitz, D., Mémin, E., Schnörr, C., 2010. Variational fluid flow measurements from image sequences: synopsis and perspectives. *Exp. Fluids* 48 (3), 369–393.
- Helman, U., Loutan, C., Rosenblum, G., Rothleder, M., Xie, J., Zhou, H., 2010. Integration of renewable resources: operational requirements and generation fleet capability at 20% rps. California Independent System Operator.
- Hoff, T.E., Perez, R., 2012. Modeling PV fleet output variability. *Sol. Energy* 86 (8), 2177–2189.
- Horn, B.K., Schunck, B.G., 1981. Determining optical flow. *Artif. Intell.* 17 (1), 185–203.
- Huang, H., Xu, J., Peng, Z., Yoo, S., Yu, D., Huang, D., Qin, H., 2013. Cloud motion estimation for short term solar irradiation prediction. In: *Smart Grid Communications (SmartGridComm)*, 2013 IEEE International Conference on. pp. 696–701.
- Jacobs, N., Islam, M. T., Workman, S., 2013. Cloud motion as a calibration cue. In: *Computer Vision and Pattern Recognition (CVPR)*, 2013 IEEE Conference on. pp. 1344–1351.
- Lave, M., Kleissl, J., 2013. Cloud speed impact on solar variability scaling – application to the wavelet variability model. *Sol. Energy* 91, 11–21.
- Liu, C., 2009. Beyond pixels: exploring new representations and applications for motion analysis. Doctoral dissertation, Massachusetts Institute of Technology.
- Liu, S., Wang, C., Xiao, B., Zhang, Z., Cao, X., 2013. Tensor ensemble of ground-based cloud sequences: its modeling, classification, and synthesis. *IEEE Geosci. Remote Sens. Lett.* 10, 1190–1194.
- Lorenz, E., Hammer, A., Heinemann, D., 2004. Short term forecasting of solar radiation based on satellite data. In: *Proc ISES Europe Solar Congress EUROSUN2004*, Freiburg, Germany.
- Lucas, B.D., Kanade, T. 1981. An iterative image registration technique with an application to stereo vision. In: *IJCAI*. Vol. 81, pp. 674–679.
- Marquez, R., Coimbra, C.F., 2013. Intra-hour DNI forecasting based on cloud tracking image analysis. *Sol. Energy* 91, 327–336.
- Menzel, W.P., 2001. Cloud tracking with satellite imagery: from the pioneering work of Ted Fujita to the present. *Bull. Am. Meteorol. Soc.* 82 (1), 33–47.
- Perez, R., Kivalov, S., Schlemmer, J., Hemker Jr, K., Renné, D., Hoff, T.E., 2010. Validation of short and medium term operational solar radiation forecasts in the US. *Sol. Energy* 84 (12), 2161–2172.
- Quesada-Ruiz, S., Chu, Y., Tovar-Pescador, J., Pedro, H.T.C., Coimbra, C.F.M., 2014. Cloud-tracking methodology for intra-hour DNI forecasting. *Sol. Energy* 102, 267–275.
- Shields, J.E., Karr, M.E., Johnson, R.W., Burden, A.R., 2013. Day/night whole sky imagers for 24-h cloud and sky assessment: history and overview. *Appl. Opt.* 52 (8), 1605–1616.
- Sundaram, N., Brox, T., Keutzer, K., 2010. Dense point trajectories by GPU-accelerated large displacement optical flow. In: *Computer Vision – ECCV 2010*. Springer, Berlin Heidelberg. pp. 438–451.
- Szeliski, R., 2010. *Computer Vision: Algorithms and Applications*. Springer.
- Urquhart, B., Ghonima, M., Nguyen, D., Kurtz, B., Chow, C.W., Kleissl, J., 2013. Sky-imaging systems for short-term forecasting. In: Kleissl, J. (Ed.), *Solar Energy Forecasting and Resource Assessment*. Academic Press, pp. 195–232.
- Urquhart, B., Kurtz, B., Dahlin, E., Ghonima, M., Shields, J.E., Kleissl, J., 2014. Development of a sky imaging system for short-term solar power forecasting. *Atmos. Meas. Tech. Discuss.* 7 (5), 4859–4907.
- West, S.R., Rowe, D., Sayeef, S., Berry, A., 2014. Short-term irradiance forecasting using skycams: motivation and development. *Sol. Energy* 110, 188–207.
- Yang, H., Kurtz, B., Nguyen, D., Urquhart, B., Chow, C.W., Ghonima, M., Kleissl, J., 2014. Solar irradiance forecasting using a ground-based sky imager developed at UC San Diego. *Sol. Energy* 103, 502–524.